

LUDWIG-MAXIMILIANS-UNIVERSITÄT MÜNCHEN

Faculty of Physics
AI in Physics Research Group

PP

Group A

Vyron Arvanitis
Emanuele Poggi
Paul Hofmann
Moritz Heidtmann
Angelos Aslanidis

Supervisor

Nikolai Krug

August 3, 2025

Contents

1	Introduction	2
2	The Belle experiment	2
2.1	Problem Description	3
3	Theory	5
3.1	Deep Sets	5
3.2	Graph Convolutional Neural Networks	5
3.3	Multi Layer Perceptron	6
3.4	Transformer	6
4	Methodology	7
4.1	The Dataset	8
4.2	Varying Layers in the DeepSet model	9
4.3	Exploiting Rotational Symmetry	10
4.4	Transforming the feature values	10
4.5	Unnecessary Features	11
4.6	Overfitting and Mitigation Techniques	12
4.6.1	Hyperparameter Optimization	13
4.7	Speedup	13
4.8	ROC Curve and AUC Evaluation	14
5	Models Used in the End	15
5.1	General setup	15
5.2	DeepSet Model	15
5.3	Combined Model	16
5.4	DeepSet with GCN	16
5.5	Combined Deepset with GCN	16
5.6	Combined Deepset with GCN Normalized	17
5.7	Transformer Model	17
5.8	Optimal Model	18
6	Results	18
6.1	ROC curves and speedup results	18
7	Conclusion	20
A	Code Listings	21
A.1	Normalization function	21

1 Introduction

In this lab course, we work with simulated data from the Belle II experiment to develop a fast and efficient simulation pipeline. The goal is to train and compare machine learning models that can predict early in the simulation chain whether an event is likely to survive later selection stages. This allows us to discard unimportant background events early, saving computational resources typically spent on full detector simulation and reconstruction (processes which are far more computationally expensive). The strategy is illustrated in Fig. 1, where a neural network acts as a pre-filter to speed up the overall simulation process.



Figure 1: Smart simulation strategy: a neural network filters generated events before expensive detector simulation. Figure adapted from the official LMU AI Lab repository [6].

2 The Belle experiment

The Belle experiment is a so-called *B-Factory*, a type of particle accelerator specifically designed to produce large numbers of *B mesons*. These factories operate with a center-of-mass energy tuned to the $\Upsilon(4S)$ resonance, a state that decays almost exclusively into pairs of B and \bar{B} mesons. This production mechanism enables detailed studies of B meson decays, allowing physicists to investigate phenomena such as *CP violation*, rare decays, and physics beyond the Standard Model. The Belle II experiment, located at the *SuperKEKB collider in Tsukuba, Japan*, is the successor to the original Belle experiment and significantly improves on its precision and data collection capabilities.

Unlike proton-proton colliders (such as the LHC), Belle II uses electron-positron (e^+e^-) collisions. Electrons and positrons are elementary particles with no internal structure, this offers several advantages. First, their interactions are much cleaner, and the background is easier to interpret—there is a notable absence of hadronic activity such as jets. Moreover, the absence of internal substructure allows us to precisely know the initial momenta of the colliding particles, enabling accurate reconstruction of the event kinematics. This precision is crucial for tuning the aforementioned center-of-mass energy to specific resonances, such as the $\Upsilon(4S)$.

B mesons are unstable particles that decay via the weak interaction, and their decays can be classified into three categories: hadronic, semileptonic, and rare decays. In *hadronic decays*, the B meson decays into only hadrons, such as combinations of kaons (K), pions (π), and other mesons. *Semileptonic decays* involve both hadrons and leptons, typically resulting in a final state containing a charged lepton (e^\pm or μ^\pm), a neutrino, and hadrons. *Rare decays* may involve photons, multiple leptons, or other suppressed processes that are especially sensitive to

effects beyond the Standard Model. These decay modes provide a rich ground for studying CP violation, flavor physics, and potential new physics.

The Belle II detector is structured as a layered system of subdetectors (like an onion) built around the interaction point. Closest to the interaction region is the Vertex Detector (VXD), composed of the PiXel Detector (PXD) and Silicon Vertex Detector (SVD), which provide precise tracking information for reconstructing decay vertices. Surrounding the VXD is the Central Drift Chamber (CDC), responsible for tracking charged particles and measuring their momenta and energy loss. Particle identification is handled by the Time Of Propagation (TOP) detector in the barrel region and the Aerogel Ring Imaging Cherenkov (ARICH) detector in the forward region. Photons and electrons are measured in the Electromagnetic Calorimeter (ECL) via the production of showers, while muons and long-lived neutral kaons (K_L^0) are identified in the outermost KLong and Muon (KLM) detector. The entire setup is enclosed in a 1.5 T magnetic field provided by a superconducting solenoid, which not only aligns the beams but also enables accurate momentum measurements. An overview of the collider (figure 2) and the particles that can be identified in each subdetector can be seen in table 1



Figure 2: Closeup of the Belle II detector indicating all the different subdetectors [2].

Subdetector	Main Purpose
PXD + SVD (VXD)	Track reconstruction near the IP, measures short-lived particles
CDC	Tracking of charged particles
TOP / ARICH	Particle identification (e.g. distinguish π , K , p) via Cherenkov radiation
ECL	Detection of electrons and photons (electromagnetic showers)
KLM	μ identification and detection of K_L^0

Table 1: Belle II subdetectors and the particles they primarily detect.

2.1 Problem Description

The Belle II experiment collects an enormous amount of data, with its center-of-mass energy tuned to the $\Upsilon(4S)$ resonance *corresponding to a center-of-mass energy of $\sqrt{s} = 10.58 \text{ GeV}$* .

While these "resonant" events are the primary source for B physics, Belle II also records other types of data.

To achieve this center-of-mass energy the two beams colliding have respective energies of 7 GeV and 4 GeV. This assymmetric beam configuration introduces a forward boost to the CoM system, forcing the produced B (and \bar{B}) mesons to travel measurable distances in the detector before they decay.

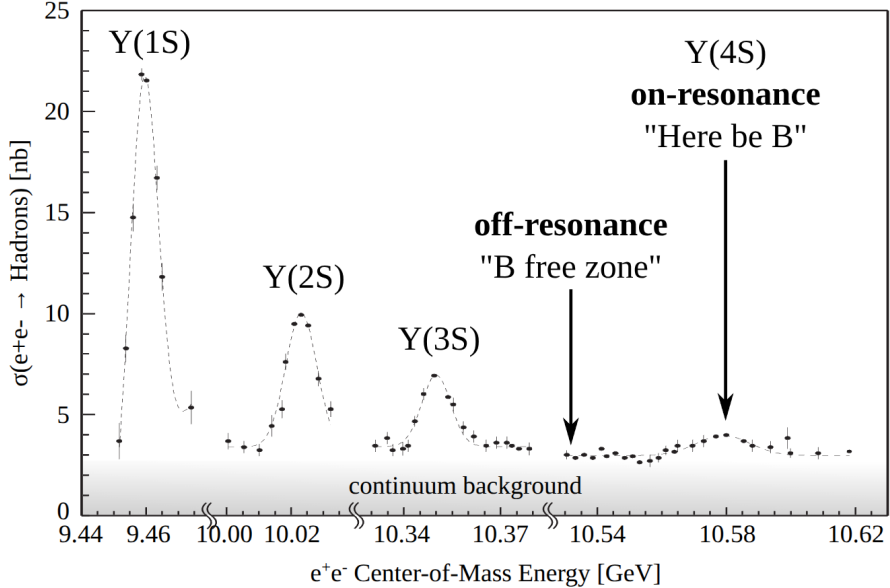


Figure 3: Cross section of e^+e^- with respect to the center-of-mass energy [GeV] [3].

To reduce the data volume and focus on interesting events, Belle II employs a two-level filtering system: the Level-1 hardware trigger (TRG) and the High Level Trigger (HLT), which together reduce the event rate before data is stored. Even after this, the number of events retained is still too large for direct analysis, so further selection — known as skimming — is performed to extract smaller datasets.

In parallel, Monte Carlo (MC) simulations are used to model the detector response and to train and validate analysis strategies. These simulated events must pass through all stages of detector simulation, digitization, reconstruction, and selection, mirroring the real data processing pipeline. However, this process is computationally expensive, especially when simulating large background samples, most of which are eventually discarded by skims.

To address this issue, the goal of this lab course is to explore a technique known as *Smart Background Simulation*. Instead of fully simulating every event, we aim to train a neural network that can predict early on whether a given event will survive a later skim. This skim selects events in which at least one B^0 meson can be reconstructed through hadronic decays. After building several neural networks we evaluate their performance on an independent test set and calculate the speedup offered by each network.

3 Theory

3.1 Deep Sets

In many physical systems, such as collections of particles or events in high-energy physics, the data can be naturally represented as unordered sets. Traditional neural networks, however, are not inherently permutation-invariant. This means that they assume an order in their input. To address this, Deep Sets provide a principled way to process such set-structured data while maintaining invariance to the order of elements. Figure 4 visualizes the structure of a Deep Set model.

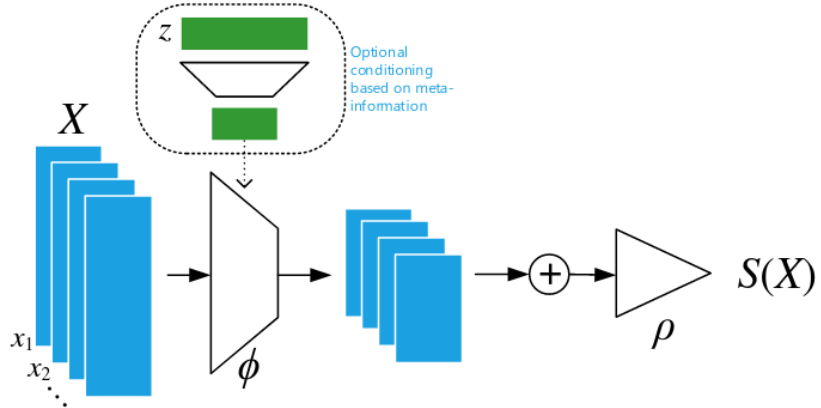


Figure 4: Schematic illustration of a Deep Set model.

A Deep Set model operates by applying a shared function ϕ independently to each element in the set. This produces a new set of embeddings, which are then aggregated using a permutation-invariant operation such as sum, mean, or max. The aggregated result is passed through a second function ρ , typically implemented as a multilayer perceptron (MLP), to produce the final output:

$$f(X) = \rho \left(\sum_{x \in X} \phi(x) \right) \quad (1)$$

This structure ensures that the model respects the symmetry of sets. The theoretical foundation of Deep Sets is discussed in [9], where it is shown that any function on a set that is invariant to permutations can be decomposed in this form.

In our project, we use this architecture to model collections of particles, where the order of particles is physically irrelevant. The Deep Set model thus provides a natural and efficient baseline for learning from such data.

3.2 Graph Convolutional Neural Networks

In contrast to Deep Set models, which treat the input as an unordered collection, Graph Neural Networks (GNNs) explicitly leverage relational information between data points. This is partic-

ularly important in our context, where particles are connected through a decay tree structure that naturally forms a graph. Each node in the graph represents a particle, and edges represent physical relationships (e.g., parent-child connections in the decay chain).

In terms of Deep Sets, graph convolutions can be seen as permutation equivariant operations. As long as the aggregation function (e.g., sum, mean, or max) is symmetric, the update remains invariant to the ordering of neighbors.



Figure 5: Analogy between CNNs and GCNs. In CNNs, pixels are updated based on spatial neighborhoods; in GCNs, nodes are updated based on graph neighborhoods.

Figure 5 illustrates the analogy between Convolutional Neural Networks (CNNs) and Graph Convolutional Networks (GCNs). In CNNs, pixels are updated based on their spatial neighborhoods, while in GCNs, nodes are updated based on their graph neighborhoods. This allows GNNs to capture complex relationships and dependencies in the data, making them particularly suitable for tasks involving structured data like particle decays.

3.3 Multi Layer Perceptron

The Multi Layer architecture is as

3.4 Transformer

The Transformer architecture was introduced by Vaswani [8]. The key ingredient in the success of the Transformer is the *self-attention* mechanism, which enables the model to capture long-range dependencies between elements of the input.

The encoder takes the input sequence (in our case, the set of particles in an event), maps tokens such as PDG identifiers to dense embedding vectors, adds positional encodings, and processes them through multiple layers of multi-head self-attention and feedforward sublayers. Each encoder layer contains connections and layer normalization, allowing information to propagate effectively through the network. In our architecture, only the encoder component of the Transformer is used, as our task is classification rather than sequence generation.

The outputs of the decoder are generated by attending both to the encoder outputs and to its

own previously generated tokens. It introduces a *masked* self-attention mechanism to prevent the model from attending to future positions in the output sequence. Since our problem does not involve generating sequences, the decoder component is omitted in our implementation.

The attention mechanism computes a weighted sum of vectors, where the weights are determined by the similarity between a query vector and a set of key vectors. In the multi-head self-attention setting, several independent attention “heads” are computed in parallel, allowing the model to focus on different types of relationships simultaneously. Self-attention enables each particle to directly incorporate information from all others in the event. The aforementioned property makes the transformer architecture highly suitable for particle physics tasks!

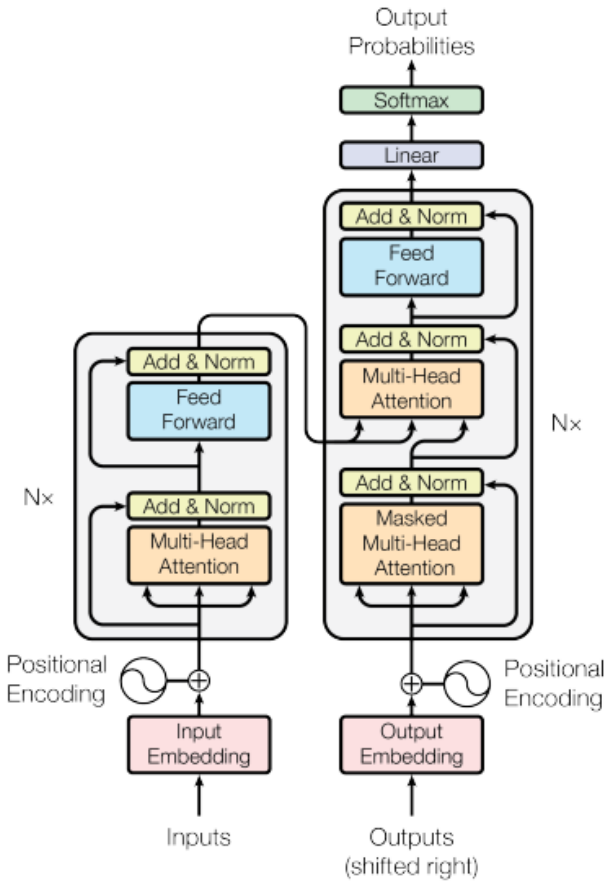


Figure 6: Transformer-model architecture [8]

4 Methodology

To identify the optimal model architecture, each group member conducted small-scale investigations targeting specific aspects of the model design. These investigations included the following:

- Does it help to increase the number of linear layers? Which sequence of GCN and Linear layers works best? 4.2
- Is it possible to use a standard MLP as well? If yes how?

- How important is the masking in this case?
- Methods to combat overfitting
- Do we need to transform the values for the particle features? [4.4](#)
- Are there any redundant features in the dataset that could be removed? [4.5](#)
- Could one make use of some (approximate) symmetries in the data? [4.3](#)
- Ideas for different model architectures

4.1 The Dataset

The dataset of the experiment consists of simulated particle collision events, with each event containing multiple decay particles. These events contain a variable number of final state and intermediate particles. Hence, they can be structured as a graph, where each particle is a node and the edges represent the relationships between particles (e.g., parent-child relationships in decays). The graph can be seen in figure [7](#).

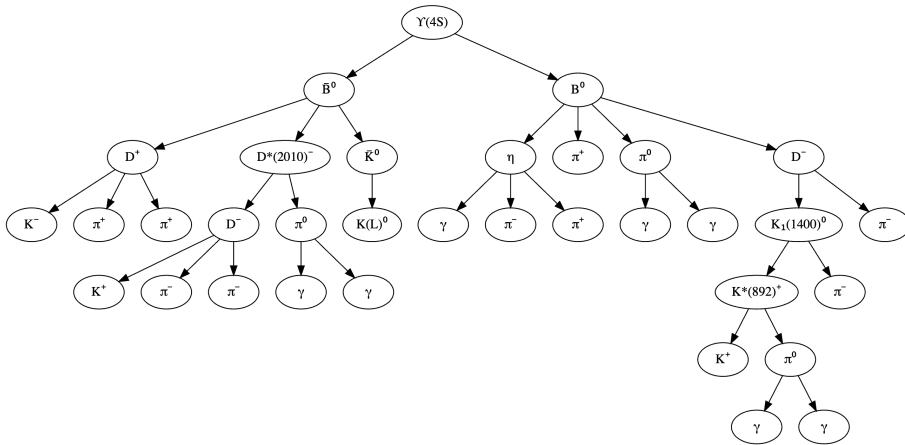


Figure 7: Example of a particle decay graph. The nodes represent particles, and the edges represent the decay relationships between them.

Each particle is described by a fixed number of features, which include:

- `prodTime` — the production time of the particle,
- `energy` — the energy of the particle,
- `x, y, z` — the spatial coordinates of the particle at production,
- `px, py, pz` — the momentum components of the particle,
- `pdg` — the PDG identifier of the particle, indicating its type,
- `index, mother_index` — the particle's index and the index of its mother particle (if any).
- `label` — this indicates whether or not the particle has passed the downstream event selection or not, it takes binary values 0 or 1

Each event is represented as a tensor of shape `(num_particles, num_features)`. Since the number of particles can vary between events, padding is applied to ensure consistent input dimensions across batches. These padded values are properly masked during training to prevent them from affecting the model.

4.2 Varying Layers in the DeepSet model

The architecture was developed to explore the optimal number and arrangement of GCN and linear layers. To support this flexibility, an additional script (`deepset_gcn_variator.py`) was introduced. This script allows dynamic model construction and naming based on the layer configuration.

The naming convention follows the pattern:

`DS_{TotalLayers}_GCN_{GCNIndices}`.

For example, the model `DS_6_GCN_135` consists of six layers (including input and output), with the 1st, 3rd, and 5th layers implemented as GCN layers. All other layers default to linear.

This models introduces two additional configuration arguments:

- `hidden_layers` (int): Number of hidden layers. The total number of layers is `hidden_layers` + 3 (one input and two output layers)
- `gcn_layers` (list): A list of layer indices to be implemented as GCN layers. For example `gcn_layers = [2,4]` replaces the 2nd and 4th layers with GCNs.

Layer behaviour is defined as follows:

- If index 1 is included in `gcn_layers`, the input layer is implemented as a GCN; otherwise, it is a linear layer.
- Hidden layers not specified in `gcn_layers` are standard linear layers.
- After all hidden layers, aggregation is performed using masked mean pooling (or mean over N if no mask is provided).
- The final output module consists of two linear layers separated by a ReLU activation (i.e., a small MLP).

The complete architecture is summarized in table 2.

Table 2: Architecture of the variable DeepSet model with configurable GCN and Linear layers

Layer #	Description	Output shape	Parameters
1	Input layer (GCN or Linear with ReLU)	$[B, N, u]$	$u \times f + u$
2 - (h+1)	Hidden layers (GCN or Linear with ReLU)	$[B, N, u]$	$u \times u + u$ (per layer)
h+2	Masked mean pooling (or mean over N)	$[B, u]$	—
h+3	Linear + ReLU (global MLP)	$[B, u]$	$u \times u + u$
h+4	Linear (output layer)	$[B, 1]$	$1 \times u + 1$

After performing multiple calculations with this architecture (see folder `saved_models/Layers_investigation`), the best model was `DS_4_GCN_123`: 4 hidden layers, with GCNs at the input, second and third

layer.

4.3 Exploiting Rotational Symmetry

Ideally, the collision of the electrons occurs parallel to the walls of the detector. This setup allows one to introduce cylindrical coordinates and exploit rotational symmetry around the z axis. In this coordinate system, the angular component can be neglected, and the transformation is defined as

$$r = \sqrt{x^2 + y^2}, \quad \text{and} \quad p_{xy} = \sqrt{p_x^2 + p_y^2}. \quad (2)$$

Here, r denotes the radial position, and p_{xy} is the transverse momentum in the xy plane. This transformation reduces the feature vector by two dimensions, thereby lowering the risk of overfitting without discarding relevant information about the particle collision.

The implementation requires an additional function, `transform_to_cylindrical`, located in `utils.py`. This function takes a DataFrame as input, which must contain at least the features '`x`', '`y`', '`px`', and '`py`'. The output is a modified DataFrame in which the original features are replaced by '`r`', and '`p_xy`'.

To enable coordinate transformation, the function `preprocess` in `utils.py` takes an additional argument, "`coordinates`", which can be set to "`cylindrical`". If this argument is not specified, the data is processed using the original Cartesian coordinates.

Theoretically, one would expect improved performance by reducing the number of parameters by compressing essential information into a more compact format using cylindrical coordinates, while discarding unnecessary information by neglecting the angular coordinate. To test this hypothesis, the models `deepset`, `deepset_gcn`, and `deepset_combined` were trained using both Cartesian and cylindrical coordinate representations.

Training was performed on all four row groups of the training set over 10 epochs, using a 75%/25% train-validation split, a batch size of 256, and early stopping with a patience of 5.

Table 3: Validation metrics for Cartesian vs. cylindrical coordinates

Model	Cartesian		Cylindrical	
	Loss	Accuracy	Loss	Accuracy
<code>deepset</code>	0.6294	63.88 %	0.6219	64.69 %
<code>deepset_gcn</code>	0.6235	64.79 %	0.6119	66.21 %
<code>deepset_combined</code>	0.4767	77.04 %	0.4727	77.43 %

4.4 Transforming the feature values

For this investigation, we used our best model obtained after the first lab day — that is **CombinedModel with GCN** model — and focused on normalizing the inputs. The implementation details can be found in Appendix A.1.

Essentially, subtracting the mean and dividing by the standard deviation of each feature, calculated across both the batch and particle dimensions.

4.5 Unnecessary Features

To investigate whether or not some features are unnecessary in our analysis, we used again the same model (**CombinedModel with GCN**) and evaluated it, subtracting features via physical arguments. We performed six tests.

First of all, we removed the momentum vector (\vec{p}). The argument for this was that the energy and momenta of a particle are associated with the well-known relationship:

$$E^2 = p^2 + m^2$$

so, in principle, the model could reconstruct the momenta from the energy (or vice versa), assuming the mass is constant or implicitly learned.

For the same reason mentioned above, we explored removing the energy of the particles.

Afterwards, we removed the position vectors x , y , and z . This started as a simple test, however the following argument was made: in our problem, there exists a cylindrical symmetry — the x and y axes can be arbitrarily chosen (as the beams are considered to be colliding along the z axis). Therefore, we considered removing only the x and y coordinates.

However, after consideration we came to the conclusion that this is physically wrong because removing both x and y would eliminate any information about the transverse plane. Therefore, we opted to remove only the x position coordinate, as a compromise to test sensitivity to symmetry arguments.

In the end, we removed the `prodTime` feature just for further analysis, since its physical importance was unclear and we wanted to check if it had any significant impact on performance.

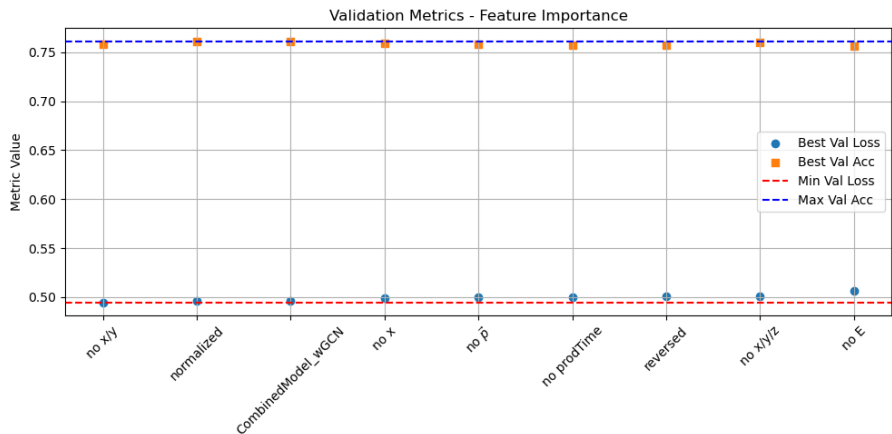


Figure 8: Validation accuracy and loss for different experiments. The horizontal dashed lines indicate the best performance achieved with the baseline model. Note: the **reversed** model refers to the configuration where the GCN and DeepSet layers were swapped.

From figure 8 it is evident that no significant improvement in model performance was observed when removing features. In all cases, the validation accuracy and loss remained close to the

baseline values. The only slight performance gain was observed when applying normalization to the input features, confirming its importance as a preprocessing step.

4.6 Overfitting and Mitigation Techniques

Overfitting occurs when a model learns not only the underlying patterns in the training data but also noise or statistical fluctuations that do not generalize to new, unseen data. This results in low training loss but poor performance on validation or test sets. In high-energy physics tasks, overfitting can severely undermine the model’s ability to detect meaningful physical signatures, especially in the presence of detector noise and variable event topologies.

To combat overfitting, we employed several regularization strategies that improve generalization:

Early Stopping

Early stopping halts training when the validation loss stops improving, even if the training loss continues to decrease [4]. This prevents the model from over-optimizing on the training data, offering a simple yet effective guard against overfitting.

Batch Normalization

Batch normalization normalizes the activations within each mini-batch to have zero mean and unit variance [5]. This reduces internal covariate shift and stabilizes learning, which allows for higher learning rates and often acts as an implicit regularizer, discouraging overfitting.

Dropout

Dropout randomly sets a subset of neurons to zero during training [7], forcing the network to develop redundant representations. This reduces co-adaptation of neurons and enhances robustness, as the model cannot rely on any single pathway to make predictions.

Regularization (L1/L2)

Regularization adds a penalty term to the loss function based on the magnitude of the model’s weights. L2 regularization (weight decay) discourages overly large weights by penalizing their squared magnitude. This constrains model complexity and promotes simpler, more generalizable solutions [4].

Increased Training Data

Expanding the training set—either through real data or augmentation—exposes the model to a broader range of examples, making it harder to memorize specific samples. More diverse data reduces variance and improves the model’s ability to generalize. In physics applications, techniques such as event reweighting or simulation-based augmentation can help increase effective training diversity.

Collectively, these methods reduce model variance and promote generalization, which is essential for ensuring reliable performance on physical inference tasks.

4.6.1 Hyperparameter Optimization

Hyperparameter optimization involves empirically testing different configurations that influence the learning behavior of a neural network. Key hyperparameters include the number of layers, neurons per layer, activation function, dropout rate, L2-regularization parameter (λ), and learning rate.

For this task, we employed the Optuna library [1], which uses the Tree-structured Parzen Estimator (TPE)—a Bayesian optimization algorithm. Unlike random search, TPE models the relationship between hyperparameters and the objective function (in our case, validation loss), and strategically explores regions of the hyperparameter space that are more likely to yield better results.

Search intervals were selected based on common literature values. After multiple trials, the following configuration produced the best performance:

- Dropout rate: 0.179
- Embedding dimension: 25
- Weight decay: 2.18×10^{-5}

This optimization process helped fine-tune the model’s capacity and regularization, ultimately improving generalization and performance on the validation set.

4.7 Speedup

To evaluate the efficiency of using a NN as a filter before detector simulation, we define the speedup as the ratio of time needed to process events *without* and *with* the NN, for the same number of positively selected (skimmed) events.

Let:

- t_g : time for event generation
- t_s : time for detector simulation and reconstruction
- $r = 0.05$: fraction of events passing the original skim (without NN)
- f_1 : true positive rate (TPR)
- f_0 : false positive rate (FPR)
- X : number of events generated

Further, we define:

$$\begin{aligned}
X_i &= r \cdot X \quad (\text{number of events passing skim}) \\
X_i &= f_1 \cdot X' \quad (\text{true positives from NN}) \\
\Rightarrow X' &= \frac{r}{f_1} \cdot X \quad (\text{number of events to be generated with NN}) \\
P &= f_1 \cdot X' + f_0 \cdot (1 - r) \cdot X \quad (\text{events passing NN})
\end{aligned}$$

The speedup is the ratio of total time without and with NN:

$$\text{Speedup} = \frac{X \cdot (t_g + t_s)}{X' \cdot t_g + P \cdot t_s}$$

Substituting X' and P into the equation:

$$\text{Speedup} = \frac{f_1 \cdot (t_g + t_s)}{t_g + t_s \cdot \left(f_1 + f_0 \cdot \frac{1-r}{r} \right)}$$

Finally, assuming $t_s = 100 \cdot t_g$, we simplify to:

$$\text{Speedup} = \frac{101 \cdot f_1}{1 + 100 \cdot \left(f_1 + f_0 \cdot \left(\frac{1-r}{r} \right) \right)}$$

4.8 ROC Curve and AUC Evaluation

To evaluate the performance of each model, we use the Receiver Operating Characteristic (ROC) curve, a widely adopted metric for binary classification tasks. The ROC curve plots the **True Positive Rate (TPR)** against the **False Positive Rate (FPR)**.

Definitions

- **True Positive Rate (TPR):** It measures the proportion of actual positives that are correctly identified:

$$\text{TPR} = \frac{\text{TP}}{\text{TP} + \text{FN}}$$

- **False Positive Rate (FPR):** It measures the proportion of actual negatives that are incorrectly identified as positives:

$$\text{FPR} = \frac{\text{FP}}{\text{FP} + \text{TN}}$$

The ideal model achieves a high TPR while maintaining a low FPR. The performance of a model can be quantified using the **Area Under the Curve (AUC)**. A higher AUC indicates better separability between the two classes.

Interpretation

- AUC = 1.0: Perfect classifier.
- AUC = 0.5: Random guessing.
- AUC < 0.5: Model performs worse than random (potentially inverted labels).

5 Models Used in the End

Based on our cumulative research, we identified the following models as the most promising. We also include simpler baseline architectures, as they help illustrate the impact of additional layers and regularization techniques on model performance.

5.1 General setup

All models described below take at least the following arguments:

- `num_features` (int): Number of input features
- `units` (int): Number of hidden units

To describe the shapes of the model layers, we adopt the following notation:

- B : Batch size
- N : Number of particles per event
- f : Number of input features
- u : Number of hidden units

The input to every model is given by B batches, each containing N particles, each having f features. The input shape is therefore $[B, N, f]$. Any deviation will be further specified for each model individually.

5.2 DeepSet Model

This model follows the Deep Sets framework (as introduced in Section 3.1), in which the same transformation is applied independently to each element of the input set, followed by a permutation-invariant aggregation. All other models are built upon this base architecture.

The architecture of the model is summarized in table 4.

Table 4: DeepSet Model Architecture

Layer #	Description	Output shape	Parameters
1	Linear + ReLU (shared across particles)	$[B, N, u]$	$u \times f + u$
2	Masked mean pooling (or mean over N)	$[B, u]$	—
3	Linear + ReLU (global MLP)	$[B, u]$	$u \times u + u$
4	Linear (Output layer)	$[B, 1]$	$1 \times u + 1$

5.3 Combined Model

This model extends the DeepSet architecture by introducing an eight dimensional PDG code for each particle, which is then mapped to an embedding vector. The resulting embeddings are concatenated with the original particle features before being processed by the rest of the network

The input to this model includes both the feature vector of each particle and the corresponding PDG ID vector.

The additional arguments introduced by this model are:

- `embed_dim`: Embedding dimension ($= e$)
- `num_pdg_ids`: Number of PDG ID categories ($= n_{\text{PDG}}$)

The architecture of the model is summarized in table 5.

Table 5: Architecture of the Combined Model with PDG embedding and DeepSet structure

Layer #	Description	Output shape	Parameters
1	Embedding lookup (PDG code)	$[B, N, e]$	$(n_{\text{PDG}} + 1) \times e$
2	Concatenation of features and embeddings	$[B, N, f + e]$	—
3	Linear + ReLU (shared across particles)	$[B, N, u]$	$u \times (f + e) + u$
4	Masked mean pooling (or mean over N)	$[B, u]$	—
5	Linear + ReLU (global MLP)	$[B, u]$	$u \times u + u$
6	Linear (output layer)	$[B, 1]$	$1 \times u + 1$

5.4 DeepSet with GCN

This model combines a Graph Convolutional Network (GCN) layer with the Deep Set architecture. The GCN captures local structure between particles as defined by an adjacency matrix (typically based on mother-daughter relations).

The additional input this model takes is an adjacency matrix that encodes the particles pairwise relationships. The adjacency matrix is a symmetric binary matrix that encodes

- mother-daughter and daughter-mother relationships between particles,
- as well as self-connections (i.e., diagonal entries are 1).

This structure ensures that information can flow both directions along the graph edges, while also preserving each particle's self-information during message passing in the GCN. The models architecture is summarized in 6

5.5 Combined Deepset with GCN

This model combines the architectures of the "DeepSet with GCN" (section 5.4) and the "Combined Model" (section 5.3): The PDG ID of each particle is mapped to an embedding vector and concatenated with its feature vector. The resulting enriched representation is then processes by the DeepSet-GCN architecture.

Table 6: Architecture of the Combined Model with PDG embedding and DeepSet structure

Layer #	Description	Output shape	Parameters
1	Graph Convolution (GCN)	$[B, N, u]$	$u \times f + u$
2	Linear + ReLU (shared across particles)	$[B, N, u]$	$u \times u + u$
3	Masked mean pooling (or mean over N)	$[B, u]$	—
4	Linear + ReLU (global MLP)	$[B, u]$	$u \times u + u$
5	Linear (output layer)	$[B, 1]$	$1 \times u + 1$

Additionally the input requires the PDG codes, and the adjacency matrix as mentioned in section 5.4. The architecture of the model is summarized in table 7

Table 7: Architecture of the Combined Model with PDG embedding, GCN and DeepSet structure

Layer #	Description	Output shape	Parameters
1	Embedding lookup (PDG code)	$[B, N, e]$	$(n_{\text{PDG}} + 1) \times e$
2	Concatenation of features and embeddings	$[B, N, f + e]$	—
3	Graph Convolution (GCN)	$[B, N, u]$	$u \times (e + f) + u$
4	Linear + ReLU (shared across particles)	$[B, N, u]$	$u \times u + u$
5	Masked mean pooling (or mean over N)	$[B, u]$	—
6	Linear + ReLU (global MLP)	$[B, u]$	$u \times u + u$
7	Linear (output layer)	$[B, 1]$	$1 \times u + 1$

5.6 Combined Deepset with GCN Normalized

This model extends the Combined Deepset with GCN architecture (model 5.5) by introducing a normalization of the inputs according to section 4.4.

Architecture The architecture is the same as in the case of 5.5 with an additional normalization layer.

5.7 Transformer Model

This architecture is quite different from the Graph Convolution and Deep Set approaches explored earlier. The Transformer leverages self-attention, a mechanism that enables the model to learn long-range interactions between particles — a capability particularly valuable in particle physics tasks.

The input to the Transformer model consists of both the particle feature vectors and their corresponding PDG codes. The PDG codes are first mapped to embedding vectors, which are concatenated with the original particle features. The combined representation is then projected to the Transformer’s internal dimension before being passed through a stack of Transformer encoder layers.

The additional arguments introduced by this model are:

- `embed_dim` (int): Embedding dimension ($= e$)
- `num_pdg_ids` (int): Number of PDG ID categories ($= n_{\text{PDG}}$)

- `num_heads` (int): Number of attention heads in each Transformer layer
- `num_layers` (int): Number of Transformer encoder layers
- `dropout_rate` (float): Dropout probability applied in the Transformer layers

The architecture of the Transformer model is summarized in Table 8.

Table 8: Architecture of the Transformer Model with PDG embedding

Layer #	Description	Output shape	Parameters
1	Embedding lookup (PDG code)	$[B, N, e]$	$(n_{\text{PDG}} + 1) \times e$
2	Concatenation of features and embeddings	$[B, N, f + e]$	—
3	Linear projection to Transformer units	$[B, N, u]$	$u \times (f + e) + u$
4	Transformer encoder stack	$[B, N, u]$	per-layer: MHSA + FFN
5	Mean pooling over particle dimension	$[B, u]$	—
6	Linear output layer	$[B, 1]$	$1 \times u + 1$

5.8 Optimal Model

This should probably be moved on the chapter above

6 Results

All models were trained using all four row groups from "`smartbkg_dataset_4k_training.parquet`", with a 75%-25% train-validation split. Evaluation was performed on all four row groups from "`smartbkg_dataset_4k_testing.parquet`". Each model was trained for 10 epochs with a batch size of 256 and 32 hidden units.

- deepset 5.2
- deepset combined 5.3
- deepset gcn 5.4
- deepset combined with gcn 5.5
- transformer 5.7
- deepset combined wwith gcn normalized 5.6

6.1 ROC curves and speedup results

Figures 9 and 10 present the ROC curves and speedup plots for our most promising models. We began with a simple Deep Set model (3.1) and, through a series of investigations, developed more complex architectures such as the Deep Set Combined model and the Deep Set Combined with GCN model. Our exploration culminated in a Transformer model and an “Optimal Model” configuration.

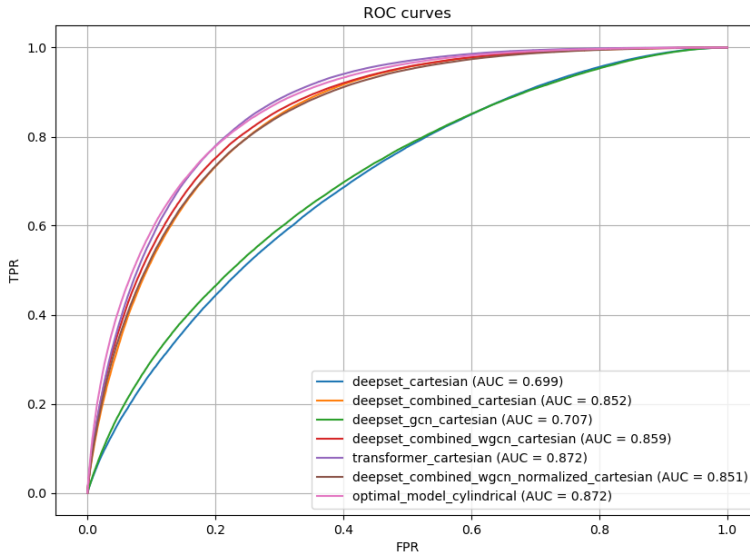


Figure 9: The resulting ROC curves of our different models

From Figure 9, it is evident that all but the simplest baseline models achieve strong results, with most AUC scores exceeding 0.85, indicating strong classification performance. The Transformer and Optimal Model stand out with the highest AUC values.

While ROC curves indicate classification quality, they do not reflect entirely the impact on computational efficiency. To address this, we also evaluate the *speedup*—(4.7) if events are filtered using the model predictions.

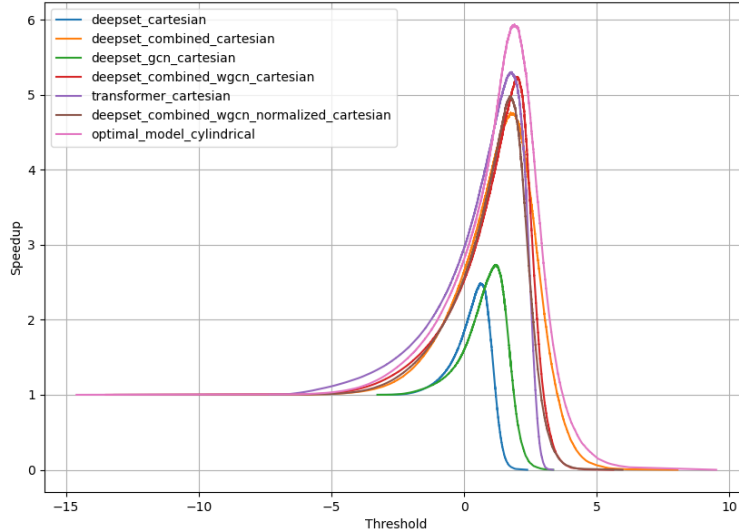


Figure 10: Speedup gained by our separate models

From figure (fig 9), we observe that the more advanced models are indistinguishable as far as their ROC performance is concerned, however they diverge in the achievable speedup. The Optimal Model attains the highest maximum speedup, followed closely by the Transformer and Deep Set Combined with GCN variants.

Table 9: Model evaluation metrics (rounded to 3 decimals)

Model	Loss	Accuracy	AUC	Max. Speedup	Best	Threshold
DS	0.633	0.636	0.699	2.485		0.618
DS_combined	0.476	0.775	0.852	4.758		1.757
DS_gcn	0.625	0.647	0.707	2.734		1.193
DS_combined_wgcn	0.467	0.779	0.859	5.236		1.993
transformer	0.441	0.795	0.872	5.301		1.774
DS_combined_wgcn_normalized	0.477	0.773	0.851	4.979		1.721
optimal_model	0.445	0.792	0.872	5.934		1.901

The *Best Threshold* column is obtained from the set of decision thresholds returned by the `roc_curve` function. These thresholds correspond to decreasing cut values on the model’s decision function that are used to compute the true positive rate (TPR) and false positive rate (FPR) pairs. The first threshold is always set to `np.inf`, which by definition yields zero predicted positives.

Among these thresholds, the one shown in the table is the value at which the model achieves its maximum estimated speedup. For example, the Optimal Model reaches a maximum speedup of 5.934 at a decision threshold of 1.901.

7 Conclusion

Appendix

A Code Listings

A.1 Normalization function

```
def normalize_inputs(inputs):
    x = inputs["feat"] # position, momentum, production time, energy
    # x.shape = (batch_size, num_particles, num_features)
    mean = x.mean(dim=(0,1), keepdim=True)
    std = x.std(dim=(0,1), keepdim=True) + 1e-8 # avoid divide-by-zero
    x_norm = (x - mean) / std
    return {**inputs, "feat": x_norm}
```

References

- [1] Takuya Akiba, Shotaro Sano, Toshihiko Yanase, Takeru Ohta, and Masanori Koyama. Optuna: A next-generation hyperparameter optimization framework. In *Proceedings of the 25th ACM SIGKDD International Conference on Knowledge Discovery and Data Mining*, 2019.
- [2] Belle II Collaboration. Belle ii detector overview. https://software.belle2.org/development/sphinx/_images/detector_labeled.jpg, 2023. Accessed: 2025-07-12.
- [3] Belle II Collaboration. Belle ii detector overview. https://software.belle2.org/development/sphinx/_images/Uresonances.svg, 2023. Accessed: 2025-07-12.
- [4] Ian Goodfellow, Yoshua Bengio, and Aaron Courville. *Deep Learning*. MIT Press, 2016.
- [5] Sergey Ioffe and Christian Szegedy. Batch normalization: Accelerating deep network training by reducing internal covariate shift. *International Conference on Machine Learning*, 2015.
- [6] Nikolai Krug. Preparation materials for particle physics lab group a. <https://gitlab.physik.uni-muenchen.de/ai-lab/ss25/pp-lab-group-a/-/blob/main/preparation.md>, 2025. Accessed: July 8, 2025.
- [7] Nitish Srivastava, Geoffrey Hinton, Alex Krizhevsky, Ilya Sutskever, and Ruslan Salakhutdinov. Dropout: A simple way to prevent neural networks from overfitting. *Journal of Machine Learning Research*, 15(1):1929–1958, 2014.
- [8] Ashish Vaswani, Noam Shazeer, Niki Parmar, Jakob Uszkoreit, Llion Jones, Aidan N. Gomez, Lukasz Kaiser, and Illia Polosukhin. Attention is all you need. *CoRR*, abs/1706.03762, 2017.
- [9] Manzil Zaheer, Satwik Kottur, Siamak Ravanbakhsh, Barnabas Poczos, Ruslan Salakhutdinov, and Alexander Smola. Deep sets. *Advances in neural information processing systems*, 30, 2017.